

Article

Deep Blind Fault Activity—A Fault Model of Strong M_w 5.5 Earthquake Seismogenic Structures in North China

Guanshen Liu ¹, Renqi Lu ^{1,*}, Dengfa He ², Lihua Fang ³, Yang Zhang ⁴, Peng Su ¹ and Wei Tao ¹¹ State Key Laboratory of Earthquake Dynamics, Institute of Geology, China Earthquake Administration, Beijing 100029, China; geoliug@163.com (G.L.); supeng@ies.ac.cn (P.S.); taowei@ies.ac.cn (W.T.)² College of Energy Resource, China University of Geosciences, Beijing 100083, China; hedengfa282@263.net³ Institute of Geophysics, China Earthquake Administration, Beijing 100081, China; flh@cea-igp.ac.cn⁴ Henan Earthquake Agency, Zhengzhou 450018, China; zy@eqha.gov.cn

* Correspondence: lurenqi@163.com

Abstract: North China is one of the high-risk areas for destructive and strong earthquakes in mainland China and has experienced numerous strong historical earthquakes. An earthquake of magnitude M_W 5.5 struck Pingyuan County, Dezhou city, in Shandong Province, China, on 6 August 2023. This earthquake was the strongest in the eastern North China Craton since the 1976 Tangshan earthquake. Since the earthquake did not produce surface ruptures, the seismogenic structure for fault responsible for the Pingyuan M_W 5.5 earthquake is still unclear. To reveal the subsurface geological structure near the earthquake epicenter, this study used high-resolution two-dimensional (2D) seismic reflection profiles and constructed a three-dimensional (3D) geometric model of the Tuqiao Fault by interpreting the faults in the seismic reflection profiles. This study further combined focal mechanism solutions, aftershock clusters, and other seismological data to discuss the seismogenic fault of the Pingyuan M_W 5.5 earthquake. The results show that the Tuqiao Fault is not the seismogenic fault of the M_W 5.5 earthquake. The actual seismogenic structure may be related to the NE-oriented high-angle strike-slip blind fault developed in the basement. We further propose three possible fault models for the strong seismogenic structure in North China to discuss the potential seismotectonics in this region.

Keywords: Pingyuan earthquake; seismogenic fault; seismic interpretation; relocation earthquakes; North China Craton



Citation: Liu, G.; Lu, R.; He, D.; Fang, L.; Zhang, Y.; Su, P.; Tao, W. Deep Blind Fault Activity—A Fault Model of Strong M_w 5.5 Earthquake Seismogenic Structures in North China. *Remote Sens.* **2024**, *16*, 1796. <https://doi.org/10.3390/rs16101796>

Academic Editors: Alessandro Bonforte, Gianluca Gropelli, Young-Seog Kim, Sambit Prasanajit Naik, Abdelrahman Khalifa and Debasis D. Mohanty

Received: 8 February 2024

Revised: 3 May 2024

Accepted: 12 May 2024

Published: 18 May 2024



Copyright: © 2024 by the authors. Licensee MDPI, Basel, Switzerland. This article is an open access article distributed under the terms and conditions of the Creative Commons Attribution (CC BY) license (<https://creativecommons.org/licenses/by/4.0/>).

1. Introduction

On 6 August 2023, an earthquake of magnitude M_W 5.5 struck Pingyuan County, Dezhou city, Shandong Province, China [1]. This earthquake was the strongest in the eastern North China Craton (NCC) since the M_S 7.8 Tangshan earthquake in 1976. The preliminary hypocentral depth of the M_W 5.5 earthquake has been estimated to be approximately 10 km (China Earthquake Networks Center, <https://news.ceic.ac.cn/>; accessed on 7 August 2023). The earthquake focal mechanism solution demonstrates clear strike-slip characteristics (Figure 1). The two sets of nodal planes strike in the NW and NE directions. The aftershock clusters are slightly distributed in the NE direction [1].

North China is one of the regions with intense seismic activity on the Chinese mainland [2–4]. Historically, there have been a total of five earthquakes with $M > 8.0$ [5]. Since 1960, strong earthquakes, such as the 1966 Xingtai M_S 7.2, 1969 Bohai M_S 7.4, 1975 Haicheng M_S 7.3, and 1976 Tangshan M_S 7.8, earthquakes have occurred, causing significant damage and loss (Figure 1) [6–8]. These events, highlighting the seismic environment and geological structures of North China, have attracted the attention of many scholars. Currently, through the study of geophysical data such as seismological data, deep seismic reflection profiles, electric structure profiles, and gravity anomalies, there is some understanding of the seismic mechanisms of strong earthquakes in the eastern part of the NCC [9–12]. A common observation in these studies is that the strong earthquakes are not associated

with the NNE–NE-oriented shovel-type normal faults formed in the cover strata but rather with blind high-angle strike-slip faults developed in the basement [6,13,14]. This is because the focal mechanism solutions of each moderate and strong earthquake exhibit distinct strike-slip properties, but the hypocenters are all situated in the basement [15,16]. However, past studies have focused on the large historical earthquakes, for with the evidence of the hypocenter location and aftershocks is weak, and the coupling or decoupling of shallow extensional normal faults with deep strike-slip faults remains unclear.

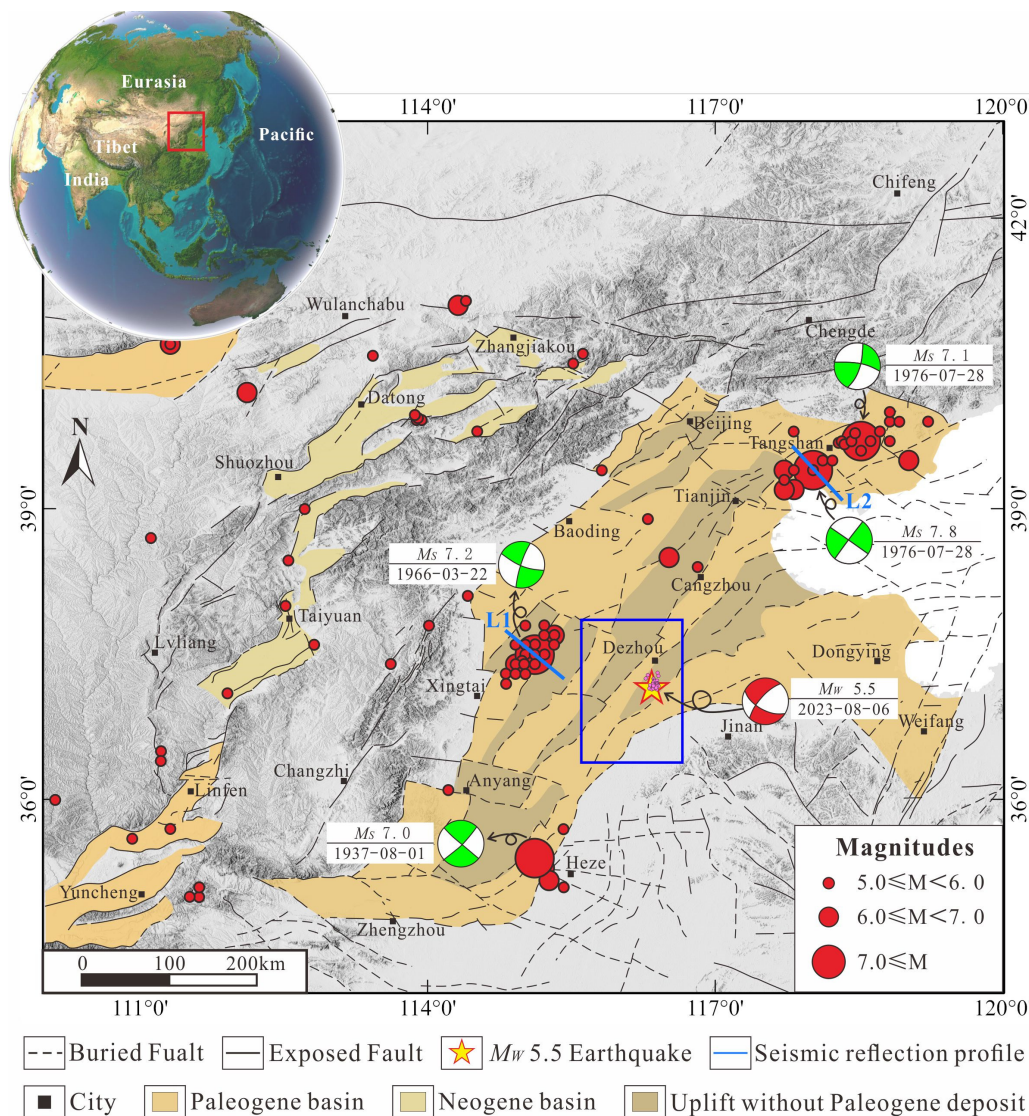


Figure 1. Geological structure map of the eastern NCC. The red dots represent the earthquakes that occurred in the eastern NCC from 1900 to 2023, and the focal mechanism solutions are all lower hemisphere projections [7,14]. The black solid lines represent faults that reach the surface, while the black dashed lines represent buried faults. The yellow pentagram represents the epicenter of the M_w 5.5 earthquake. The grayscale represents the elevation. The pink dots superimposed on the pentagram represent the aftershocks of the M_w 5.5 earthquake. The red box represents the location of the study area; the blue box represents the area where Figure 2a is located. The dark-blue solid lines L1 and L2 represent the positions of the deep seismic reflection profiles passing through the epicenters of the Xingtai and Tangshan earthquakes, respectively.

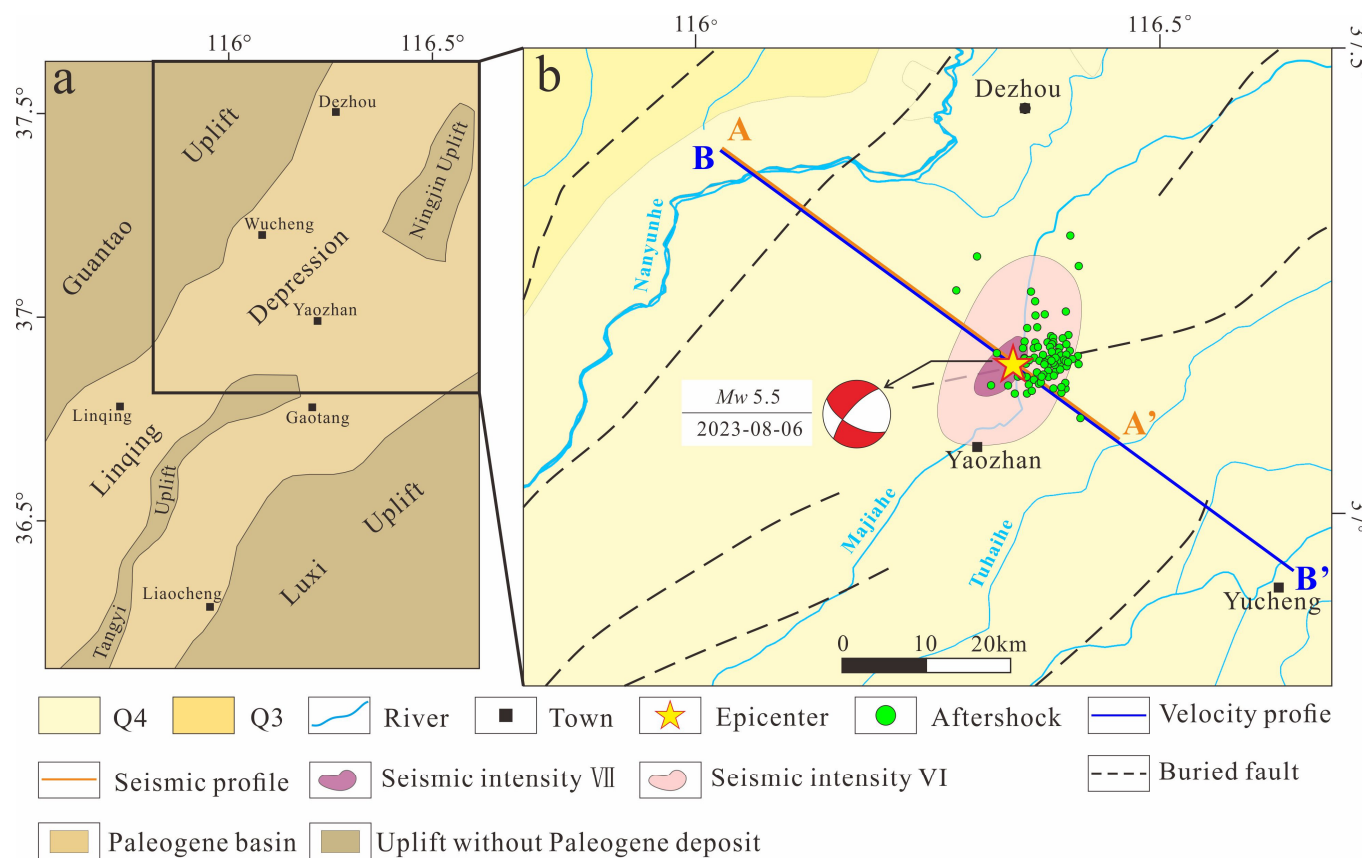


Figure 2. Geological map and seismic intensity map near the epicenter. (a) is the tectonic unit map of the Linqing Depression. (b) is the seismic intensity map. The yellow solid line represents the position of the 2D seismic reflection profile, the blue solid line represents the position of the velocity profile, the light-blue solid line represents the river, and the black square represents the city. The focal mechanism solution and aftershock relocation is cited from Zhang et al., (2024) [1]. The purple and pink ovals represent the distribution ranges of areas of different seismic intensity (<https://www.cea.gov.cn/>; accessed on 8 August 2023).

Some seismic reflection profiles obtained during petroleum exploration have indicated that the flower-shaped structures developed in the Neogene and Quaternary strata may be related to strike-slip faults in the basement [17], but the relationship between the shallow structures and deep structures remains unclear. In the eastern NCC, due to the thick sedimentary layers, the deep seismogenic structure is ambiguous, and a seismogenic fault is difficult to identify. Limited by the imperfection of earthquake monitoring equipment, there is a scarcity of detailed research data and monitoring data for the previous strong earthquakes. However, there were relatively densely fixed stations near the epicenter of the Pingyuan M_w 5.5 earthquake, providing comprehensive records of that earthquake and an opportunity to understand the seismogenic structure of the eastern NCC.

This study utilizes a high-resolution two-dimensional (2D) seismic reflection profile to analyze the subsurface structure of the M_w 5.5 earthquake zone (Figure 2) and illustrate the buried pre-existing fault system. This study further combines the focal mechanism solution and the precise location results of aftershocks to identify seismogenic faults and proposes a seismogenic structure model for strong earthquakes in the eastern NCC through the analysis of geological structures. From this perspective, information on the seismic environment in the eastern NCC, the case study here, provides a reference for assessing the earthquake risk of the region.

2. Geological and Geodynamic Setting

The study area was located in the Linqing Depression (Figure 2), which is regionally located in the eastern NCC (Figure 1). The Linqing Depression has been transformed by multiple tectonic movements along with the formation and evolution of graben basins in the eastern NCC [18,19] and exhibits various tectonic-sedimentary features (Figure 3). Within the Linqing Depression, Upper Ordovician, Silurian, Devonian, and lower Carboniferous strata are missing.

Erathem	System	Stratum Symbol	Formation	Lithology	Tectonic Movement	Legend
Cenozoic	Quaternary	Qh	Pingyuan		Himalayan Movement	
		Qp				
	Neogene	N2	Minghuazhen			
		N1	Guantao			
	Paleogene	E3	Dongying			
		E2	Shahejie			
		E1	Kongdian			
	Mesozoic	K1	Qiucheng			
		J3	Linxi			
		J2	Santai			
	Palaeozoic	J1	Fangzi			
		T2	Ermaying			
		T1	Heshanggou			
			Liujiagou			
		P3	Shiqianfeng			
	Permian		Upper Shihezi			
		P2	Lower Shihezi			
	Carboniferous	P1	Shanxi			
			Taiyuan			
	Ordovician	C3	Benxi			
		O2	Fengfeng			
			Upper Majiagou			
			Lower Majiagou			
		O1	Liangjiahsan			
	Cambrian		Yeli			
		E3	Fengshan			
			Changshan			
			Gushan			
		E2	Zhangxia			
			Xuzhuang			
			Maozhuang			
		E1	Mantou			
			Fujunahsn			

Figure 3. Lithology in the Linqing Depression. The dashed lines between the strata represent parallel unconformities, while the wavy lines represent angular unconformities.

Currently, it is widely accepted that the NCC comprises two structural systems: the extensional fault system and the strike-slip fault system [20]. These two structural systems developed during distinct geological periods. The extensional fault system primarily initiated development in the early Cenozoic and generally became inactive by the end of the Miocene [21]. The extension fault influenced basin development and established the fundamental structural framework. The strike-slip fault system has remained active since the Neogene and has been superimposed on pre-existing structures [22]. Therefore, the unconformity between the Neogene and Paleogene strata is important. It marks the period of tectonic change where the Linqing Depression transitioned from a graben to a depression [20,23]. The activity of normal faults within the depression gradually ceased, and strike-slip fault activity replaced the normal fault activity [20,24–27].

In the late Mesozoic, as the destruction of the NCC reached its peak, the Linqing Depression entered its initial graben stage. In the early Cenozoic, the entire basin on the eastern NCC entered a large-scale period of graben formation, and the Linqing Depression formed its NE-oriented structural pattern during this stage (Figure 2) [21,28,29]. In the late Cenozoic (~8 Ma), under the influence of dextral strike-slip motion, some NE-oriented faults were activated [15,16,30,31].

Seismic activity within the Linqing Depression is relatively low. The Pingyuan M_W 5.5 earthquake was the largest magnitude earthquake in the eastern NCC since the Tangshan M_S 7.8 earthquake in 1976. The areas of different seismic intensity related to this earthquake uniformly show a NE orientation laterally (Figure 2b). Therefore, under the influence of dextral strike-slip extension, NE-oriented faults within the Linqing Depression may continue to be active, causing moderate and strong earthquakes.

3. Data and Methods

In 2005, Sinopec collected many of the 2D seismic reflection profiles in the Linqing Depression, with survey lines covering the entire study area. The average main frequency of the 2D seismic reflection profile is approximately 25 Hz. Drilling data and well-seismic synthetic records within the Linqing Depression indicate that the average seismic wave velocity in the area is approximately 4000 m/s [32]. The vertical resolution of a seismic reflection profile is approximately 20 m [33]. We selected one 2D reflection profile passing through the epicenter of the M_W 5.5 earthquake (Figure 2) to construct the subsurface geological structure near the epicenter. Based on well-seismic synthetic records, different layers were calibrated to determine the time-depth conversion relationship, and the seismic reflection profile was converted from time to depth. The study also used a velocity structure model to analyze deep structures. This model collected seismic phase observation data from 211 fixed stations within the range of 29–39°N and 108–118°E, recorded from January 2008 to November 2018. The three-dimensional (3D) velocity model of the study area was provided using the double-difference tomography method [34].

We used the focal mechanism solution and aftershock location data given by Zhang et al., (2024) [1]. Zhang et al., (2024) [1] collected waveform data from 74 fixed stations within 200 km of the epicenter of the M_W 5.5 earthquake. They used the generalized polarity and amplitude technique to determine the hypocentral depth and the focal mechanism solution for this earthquake [35]. The double-difference relocation method [34] provided the locations of 97 earthquakes within 5 days after the M_W 5.5 earthquake. Finally, this study utilized SKUA-GoCAD (Version 2017) software to construct a 3D geometric model of the pre-existing faults near the earthquake hypocenter [36–38]. Then the focal mechanism solution and aftershock clustering were compared to analyze the seismogenic structure of the study area.

4. Results

4.1. Pre-Existing Fault Development

The seismic reflection profile is oriented in the NW–SE direction, perpendicular to the long axis of the seismic intensity map (Figure 2). The structural evolutionary stages

in this region are relatively complex, resulting in the development of multiple regional unconformities, which can be seen in the profile as evident truncations. The Neogene and Quaternary sediments are relatively thick, with an average depth of approximately 2 km, covering the entire region. Paleogene sediments are thicker in the central depression and gradually thin toward the edges, eventually tapering off at the base of the Neogene (Figure 4). The Mesozoic experienced multiple phases of compression and extension, as well as uneven uplift during tectonic movements [39]. This has resulted in different sedimentary thicknesses in different regions. Thrust faults formed during the Paleozoic are still preserved within the Mesozoic strata (Figure 4).

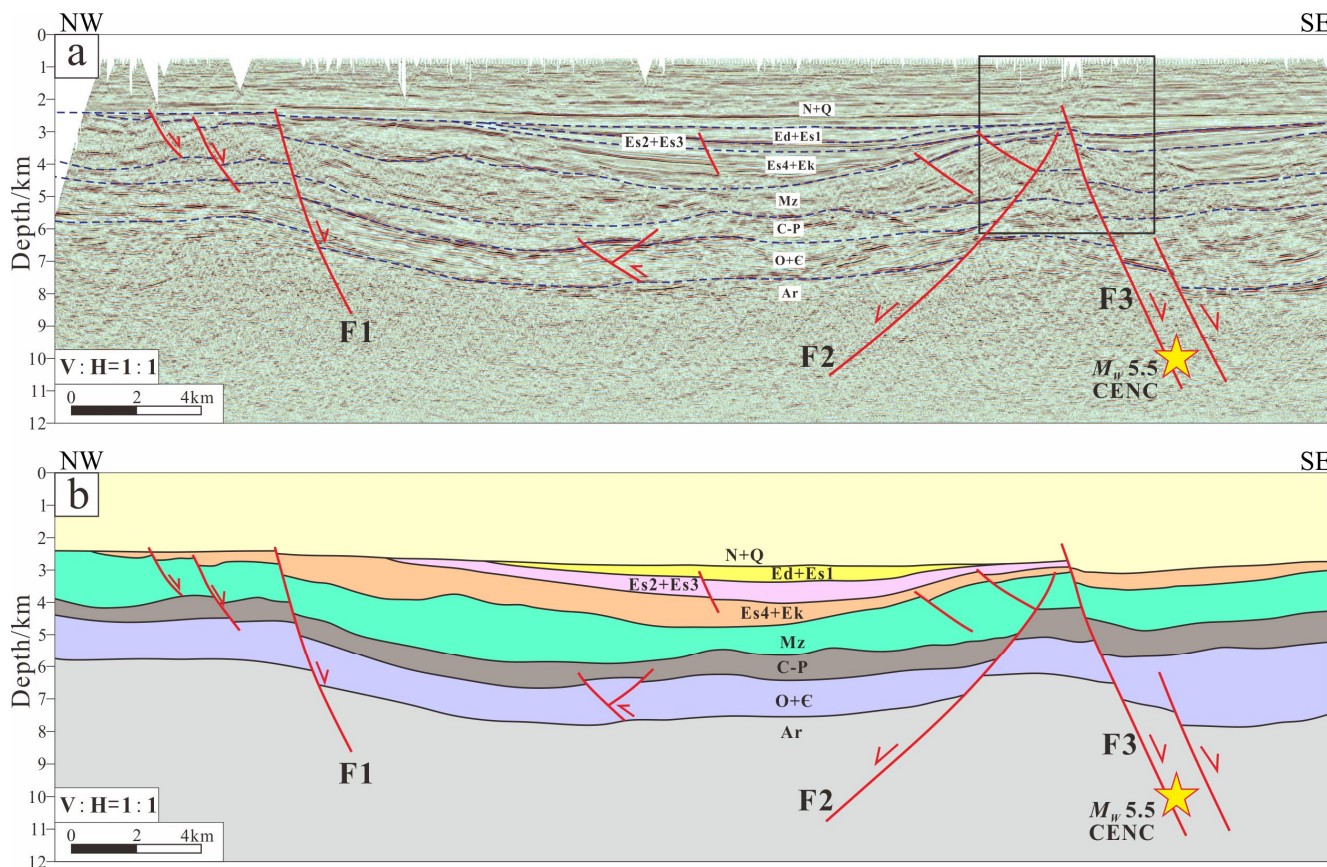


Figure 4. Seismic reflection profile AA' and its interpretation. (a) is seismic reflection profile. (b) is interpretation scheme. The yellow pentagram represents the centroid position of the M_w 5.5 earthquake. The solid red line represents the fault, and the red arrow represents the direction of movement of the fault. The black box represents the position of Figure 5. The F1 fault is the Kongzhuang Fault; F2 represents the Tuxi Fault, and F3 represents the Tuqiao Fault.

The Kongzhuang Fault (F1), Tuxi Fault (F2), and Tuqiao Fault (F3) are the main faults visible in the seismic reflection profile. All three faults are shovel-type normal faults with steeply dipping tops and gently dipping bottoms. These faults controlled the development of the Linqing Depression and the distribution of the strata within it. The Kongzhuang Fault is the western boundary of the Linqing Depression. Multiple smaller-scale secondary faults with similar tendencies developed in the footwall of the Kongzhuang Fault. The secondary faults form a step-like structural pattern, with the strata gradually descending and thickening in the SE direction along each fault. The Tuxi and Tuqiao Faults have opposite inclinations. Between these two faults, a horst structure is formed where the Mesozoic layers are noticeably thinner.

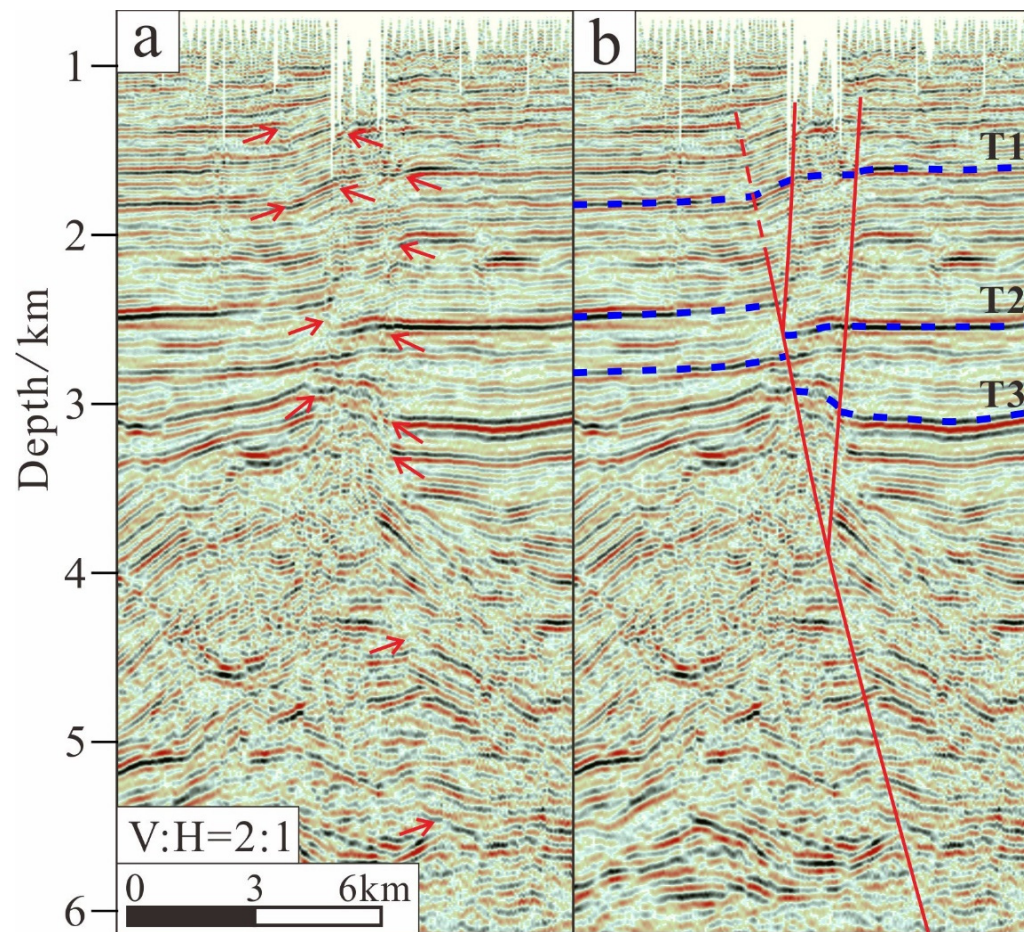


Figure 5. Partial detail of the breakpoint on the Tuqiao Fault (located in the black box of Figure 4). (a) is the seismic reflection profile. (b) is the seismic interpretation. The red solid line represents the fault, the red dashed line represents the inferred fault, and the red arrow represents the location of the breakpoint and fold. The blue dashed line represents the bottom boundary of different strata. T1 is the bottom boundary of the Neogene Minghuazhen Formation, T2 is the bottom boundary of the Neogene Guantao Formation, and T3 is the bottom boundary of the Paleogene Kongdian Formation.

The Tuxi Fault cuts through only the base of the Paleogene Kongdian Formation, indicating its older period of activity. However, both the Kongzhuang and Tuqiao Faults intersect the boundary of the Neogene strata, suggesting that these two faults were still active during the Neogene. The M_W 5.5 earthquake hypocenter, as determined by the China Earthquake Networks Center (CENC), is located within the basement, close to the Tuqiao Fault (F3), near the bottom of the fault.

To clearly show the upper breakpoint of the Tuqiao Fault, the seismic reflection profile above the Tuqiao Fault was magnified (Figure 5). Three strong reflectors in the profile were selected as marker layers. T1, T2, and T3 represent the bottom boundaries of the Neogene Minghuazhen Formation, the Guantao Formation, and the Paleogene Kongdian Formation, respectively (Figure 3). During Neogene sedimentation, the tectonic environment was relatively stable, and the strata display parallel continuous reflections in the seismic reflection profile. The bottom boundaries of the Guantao Formation and Kongdian Formation are both regional unconformities (Figure 3), which appear as continuous strong reflectors, making them easy to identify.

Due to the fault activity, deformation and displacement occurred in the strata above the fault (Figure 5a). The seismic reflection profile distinctly reveals that where the fault passes, the continuity of the reflector is compromised. The displacement between the T2 and T3 interfaces is significant, and the fault characteristics are evident (Figure 5b). In the strata above the T2 interface, there is no obvious fault displacement; instead, the strata exhibit folds. Based on the extent of these folds, it is speculated that the depth of the upper breakpoint of the Tuqiao Fault is approximately 1.3 km. Near the T1 interface, there is a structural inversion in the Tuqiao fault, manifested as an upward bulge in the overlying strata (Minghuazhen Formation). This characteristic is also reflected in the two secondary faults developed in the hanging wall of the Tuqiao Fault, displaying a compressive-twisting structural style. This indicates that the Tuqiao Fault possesses a certain strike-slip characteristic (Figure 5b). Considering that the Minghuazhen Formation developed during the upper Pliocene of the Neogene and that its bottom boundary (T1) is dated to approximately 5 Ma, the strike-slip movement of the Tuqiao Fault began at least as early as 5 Ma.

4.2. Three-Dimensional Imaging of the Tuqiao Fault

The CENC (<http://news.ceic.ac.cn> (accessed on 7 August 2023)) reported a preliminary hypocentral depth of 10 km for the M_W 5.5 earthquake, whereas Zhang et al. (2024) [1] located a hypocentral depth of 16 km. In contrast, both the United States Geological Survey (USGS) and Global Centroid Moment Tensor Project (GCMT) reported a hypocentral depth of 18 km (Table 1). Thus, there is uncertainty regarding the hypocentral depth of the earthquake. The current focal mechanism solution indicates that nodal planes I and II have NE and NW strikes, respectively, and dip approximately 70° . The focal mechanism solution suggests that the fault is a steeply dipping normal fault with a strike-slip component (Table 1).

Table 1. Hypocenter depth and focal mechanism solution of the M_W 5.5 earthquakes obtained from different sources.

Time (yyyy/mm/dd)	Depth (km)	Nodal Plane I ($^\circ$)			Nodal Plane II ($^\circ$)			M_W	Sources
		Strike	Dip	Rake	Strike	Dip	Rake		
2023/08/05	18	221	74	-158	125	69	-17	5.6	GCMT
2023/08/05	18	37	70	-171	304	81	-21	5.44	USGS
2023/08/06	16	126	70	-16	222	75	-160	5.54	Zhang et al., 2024 [1]
2023/08/06	10	/	/	/	/	/	/	/	CENC

The 3D model of the Tuqiao Fault constructed with Skua-GoCAD shows that the Tuqiao Fault strikes NE and dips to the E, with a depth range of approximately 2.5–11 km. The average dip angle of the fault is approximately 73° (Figure 6a,b). Spatially, the hypocenter of the M_W 5.5 earthquake given by CENC is at the bottom of the Tuqiao Fault. The clustering of aftershocks matches nodal plane I. However, the inclination of nodal plane I does not align with the Tuqiao Fault occurrence (Figure 6b). Other studies have provided hypocentral depths exceeding the control range of the Tuqiao Fault. Therefore, the Tuqiao Fault is not the seismogenic fault of the Pingyuan M_W 5.5 earthquake. Based on the 3D model of the Tuqiao Fault, the distribution depth of aftershocks, and the hypocentral depth, this study further supports the hypocenter location results of the USGS, the GCMT, and Zhang et al., (2024) [1].

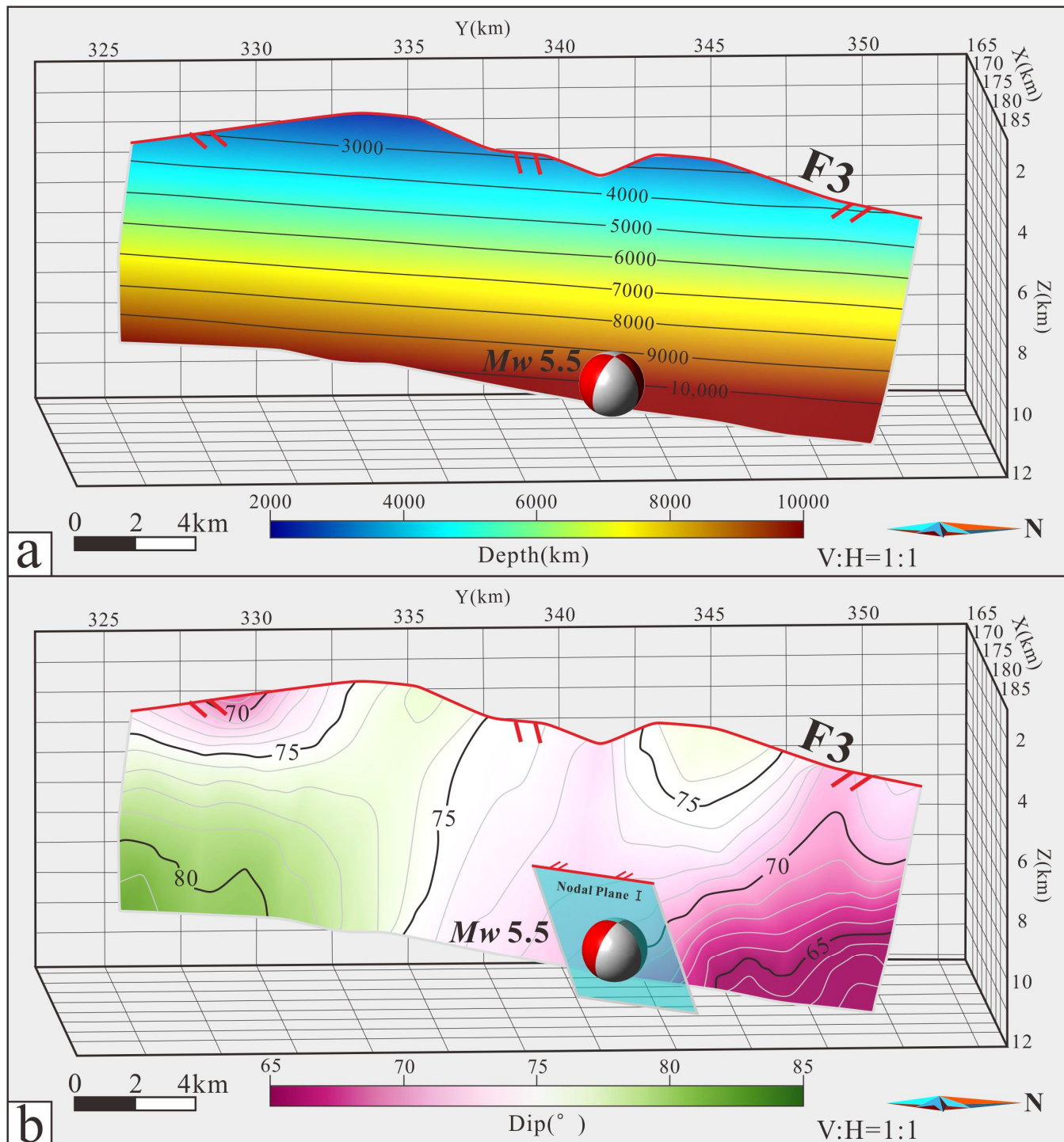


Figure 6. The 3D geometric model of the Tuqiao Fault. (a) shows the depth map of the Tuqiao Fault; (b) shows the distribution of dip angles of Tuqiao Fault. The red solid line represents the fault trace at the top of the fault, the two short red lines represent the position of the hanging wall of the fault, the gray dashed line represents the contour of the fault, and the light-blue transparent area represents nodal plane I in the focal mechanism solution.

4.3. InSAR Observation and Results

Interferometric Synthetic Aperture Radar (InSAR) is currently the most common method for reconstructing coseismic deformation fields and modeling fault slip kinematics. To capture the coseismic deformation associated with the Pingyuan earthquake, we collected pre- and post-event SAR data from the Sentinel-1 satellite of the European Space

Agency. The pre- and post-event images were respectively acquired on 5 August 2023, and 17 August 2023, with a time interval of 12 days. The differential interferogram of the SAR image pairs was obtained using GAMMA software (Version 2020) [40,41]. To avoid phase jumps between adjacent bursts in the terrain observation by progressive scan data mode, the accuracy of coregistration in the azimuth direction was better than 0.001 of a pixel [41]. The phase contributed by ground topography was calculated and removed using digital elevation data with a resolution of 30 m from the Advanced Land Observing Satellite [42,43]. The interferogram was filtered using an adaptive spectral filter method and then unwrapped using a minimum cost flow algorithm [44,45]. Finally, the unwrapped interferogram image was geocoded to the World Geodetic System 1984 geographic coordinate system.

While our surface deformation field thoroughly covers the Pingyuan earthquake fault and its epicenter from USGS and GCMT, we cannot definitively ascertain the surface deformation signals related to the earthquake (Figure 7). Along the Pingyuan earthquake fault, surface signals measure less than 2 cm in total. Despite the capabilities of InSAR observation to accurately detect centimeter- or even millimeter-scale coseismic deformation signals, we are unable to observe the surface deformation pattern caused by a predominant strike-slip fault rupture (Figure 7). Additionally, the Pingyuan earthquake fault was determined to have a ~NE126°SW strike angle, suggesting that the fault rupture primarily contributed to surface deformation dominated by north–south motion. Unfortunately, InSAR observations are not sensitive to north–south motion. Lastly, considering the depth of the epicenter constrained from seismic data exceeds 10 km and the moment magnitude is less than 5.6, InSAR observations are likely unable to detect accurate coseismic deformation signals. Consequently, despite our utilization of InSAR observations to detect the surface deformation associated with the Pingyuan earthquake, the coseismic deformation pattern remains unidentified, thus failing to provide helpful information about the fault kinematics of the earthquake.

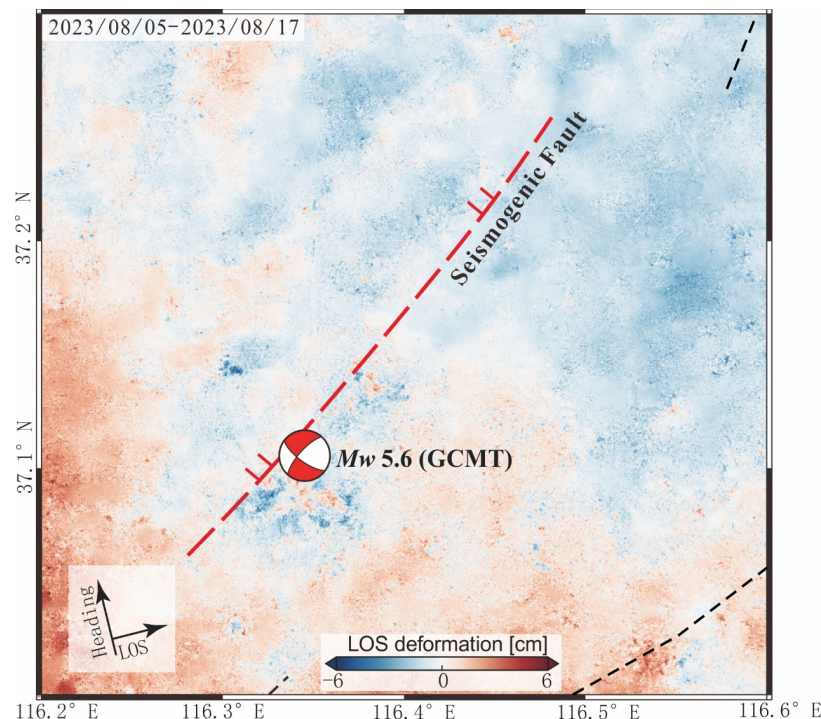


Figure 7. Surface deformation signal from our InSAR observation. The red dashed line represents the concealed seismogenic fault. The two red solid lines indicate the position of the hanging wall of the seismogenic fault. The black thin dashed lines represent pre-existing concealed faults.

5. Discussion

5.1. Relationship between Deep Structures and Seismic Activity

The Pingyuan M_W 5.5 earthquake produced 97 aftershocks over 5 days [1]. On the plane, they are distributed within 15 km of the NE and 26 km of the NW (Figure 2). The depth range of these aftershocks is 10–30 km (Figure 8). Petroleum seismic reflection profiles are limited by the depth of detection and do not cover the range corresponding to the aftershock distribution. Therefore, we discuss the deep structure of the Linqing Depression by combining the velocity profile, aftershock clusters results, and focal mechanism solution.

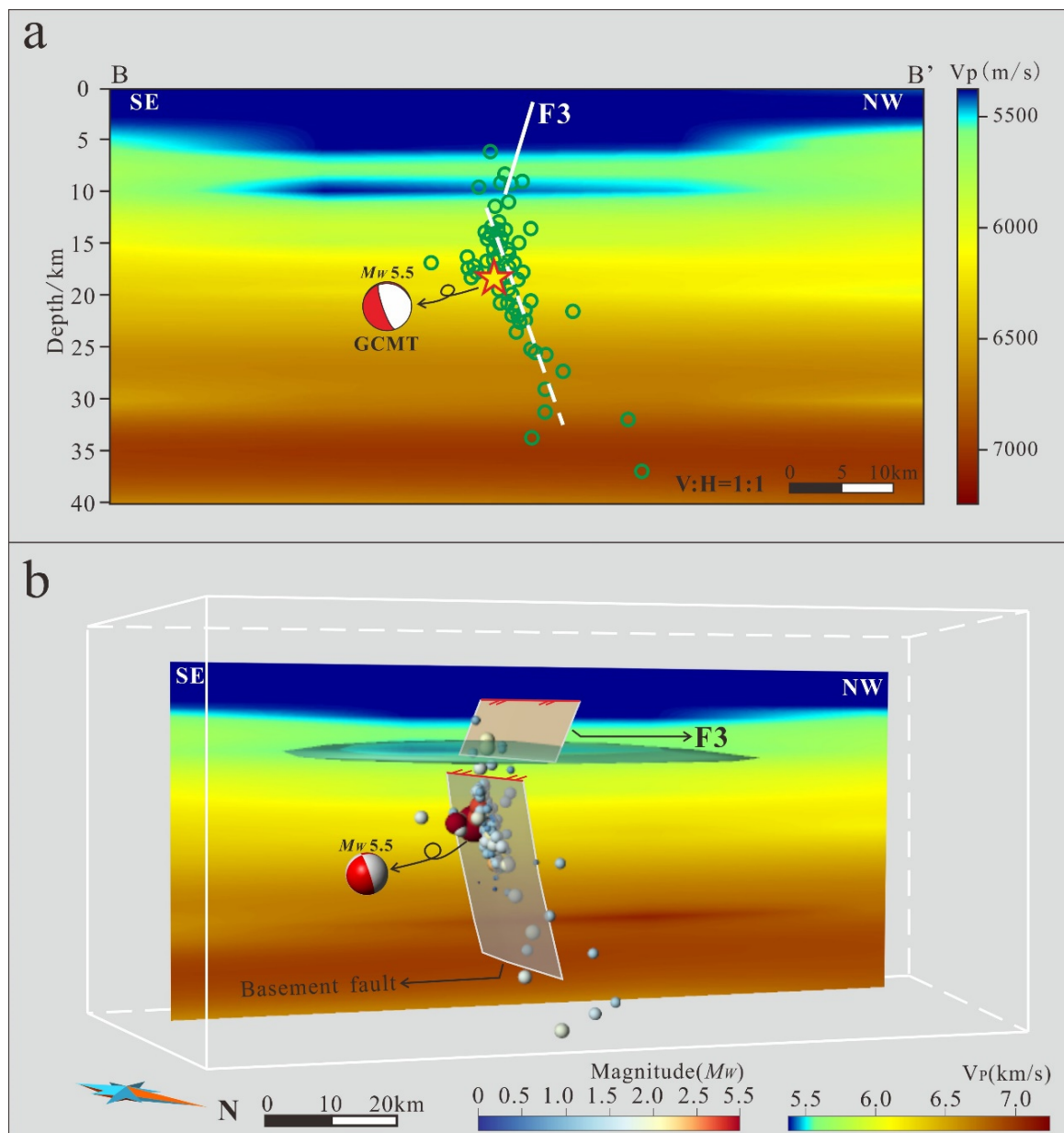


Figure 8. (a) is velocity structure profile BB'. (b) is location map of faults and earthquakes. The white dashed line represents the basement fault inferred from the cluster of aftershocks. The green circle represents the location of an aftershock. The long red solid line represents the fault trace at the top of the fault, the two short red solid lines represent the tendency of the fault, the gray dashed line represents the contour of the fault, the different colors of the sources represent different magnitudes, the different colors of the velocity data represent different velocity magnitudes, and a transparent blue area represents low-velocity body.

Overall, each velocity layer is approximately horizontally distributed, without noticeable anomalies. The low-velocity area above 5 km essentially reflects the perimeter of the Linqing Depression and the thickness of its sedimentary layers (Figure 8a). The hypocentral depths of the M_W 5.5 earthquake given by Zhang et al., (2024) [1], the USGS, and the GCMT are all approximately 18 km. Moreover, aftershocks above 10 km are sparse, and most of them are distributed within the 10–30 km range, which exceeds the range of the Tuqiao Fault. Based on the clustering of aftershocks and the focal mechanism solution, it is inferred that there is a deep-seated blind fault in the basement with a NE strike and SE dip (Figure 8a). Thus, seismic activity is likely controlled by this blind basement fault, rather than the Tuqiao Fault in the covering strata.

Notably, at an approximately 10 km depth, there is a distinct low-velocity layer, separating the listric normal faults developed in the cover strata from the high-angle strike-slip faults in the basement (Figure 8b). Such characteristics are also commonly found in other basins in the eastern NCC. This low-velocity layer is considered the boundary between the upper and lower crust [6,46,47]. The oblique distribution of the Quaternary sedimentary center around the plane and the non-coincident centers of the crustal boundary and the Moho surface indicate that the Quaternary sedimentation was controlled by recent tectonic movements. Significant interlayer slip occurred between the upper and lower crust [48–50]. Therefore, the faults in the cover and basement have different developmental periods, structural styles, and kinematic characteristics. This also explains why seismic activity has been concentrated in the basement and why the focal mechanism solution of moderate and strong earthquakes have obvious strike-slip properties (Figure 8b). Although the graben basin of the eastern NCC was dominated by normal faults in its early stage of development, the current basement faults are the main factor controlling seismic activity.

5.2. Seismotectonic Model of the Eastern Basin in North China

In recent years, through studies on the Tangshan, Xingtai, Cixian, and Heze earthquakes, two seismic genesis models have been proposed. One model describes the tectonic decoupling between the upper and lower crusts (Figure 9a) [6], while the other suggests a consistent correspondence between deep and shallow structures (Figure 9b) [11]. A common feature of both models is that the strong earthquake hypocenters are either near the boundary between the upper and lower crust or within the basement. Their relationship to the basin structure in the upper crust is minimal, and they are closely related to the high-angle strike-slip faults in the deep crust [6,11,13,14,51,52]. Based on the analysis of the fault structure of the M_W 5.5 earthquake, the strike-slip fault in the basement did not control the normal fault in the cover strata (Figure 4). Seismic reflection profiles also do not show flower structures corresponding to the basement strike-slip fault (Figures 4 and 8b). The normal faults in the cover strata and the strike-slip faults in the basement exhibit two distinct structural styles. Therefore, this study suggests that the seismogenic model for the Pingyuan earthquake aligns more with the model of tectonic decoupling between the upper and lower crust.

Based on the elliptical features of borehole wall collapses, the current stress field has a maximum horizontal principal stress orientation of N70–80°E [53]. This supports the strike-slip motion of the NNE–NE-oriented faults within the basin [19]. The GPS-based deformation field also indicates that under the combined control of the eastward push from the Qinghai–Tibet Plateau [54,55] and the subduction of the western Pacific Plate [56], the various blocks within the NCC rotate counterclockwise [15]. Some of the rotation is absorbed within these blocks by right-lateral strike-slip along the NNE–NE-oriented faults [15,16]. Hence, in the late Cenozoic, the strike-slip fault in the Linqing Depression basement with a NE orientation might have been a product of the most recent tectonic movement [3,48,57–59]. Furthermore, it governs the seismic activities in the Dezhou region [7,17]. Under the current tectonic stress field, the strike-slip fault in the Linqing Depression basement with a NE orientation is more prone to rupture, producing moderate to strong earthquakes.

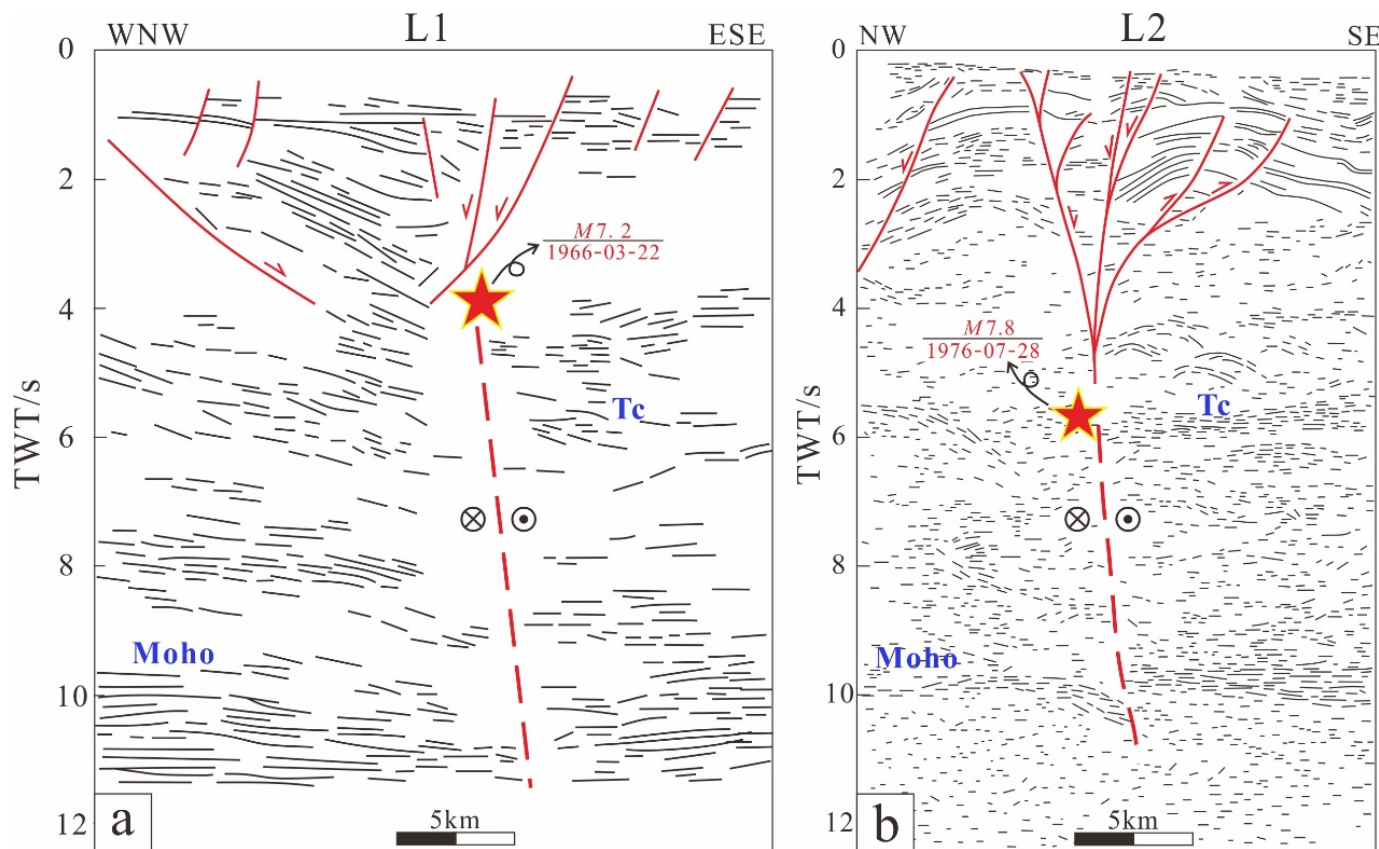


Figure 9. Seismogenic models of the Xingtai and Tangshan earthquakes in North China. (a) shows the seismogenic model of the Xingtai earthquake (modified by Wang et al., (1997) [7]); (b) shows the seismogenic model of the Tangshan earthquake (modified by Liu et al., (2011) [9]). The red solid line represents the fault, and the red dashed line represents the inferred basement fault. Tc is the boundary between the upper and lower crust. The locations of the deep seismic reflection profiles are shown in Figure 1.

Based on the above evidence, we propose a tectonic evolution model for the Linqing Depression (Figure 10). During the early Cenozoic, extensional faults within the cover strata dominated the development of the graben basin (Figure 10a). The detachment at the bottom of the basin limits the depth of normal fault development. In the late Cenozoic, the activity of normal faults gradually ceased, and high-angle strike-slip faults striking NE in the basement began to be active [20], generating seismic activity (Figure 10b). With the enhancement of strike-slip activity in the Cenozoic, flower-shaped structures related to strike-slip faulting developed in the cover strata (Figure 10c), and these strike-slip faults modified the earlier normal faults, causing the structural inversion of normal faults (Figure 10d) [22,25]. When a large earthquake occurs at the blind basement fault, stress will be released through branch faults (Figure 10c) [60] or pre-existing faults [61], forming surface fractures (Figure 10d) [11,62].

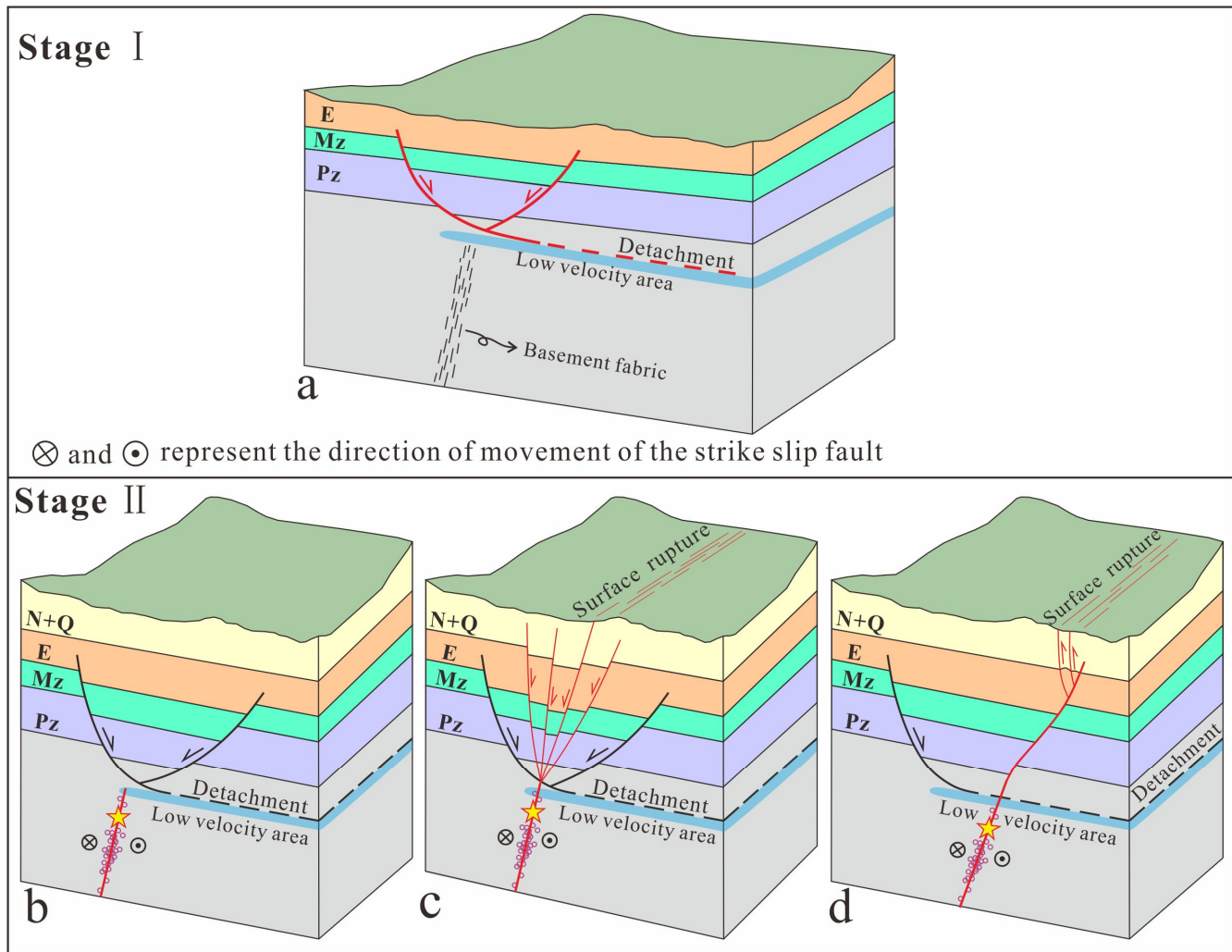


Figure 10. Tectonic evolution and current strong earthquake structural models of the eastern graben basin in North China. (a) shows the development pattern of faults during the early Cenozoic basin graben period; (b–d) show possible seismogenic patterns since the late Cenozoic. The red solid line represents the fault during the active period, the black solid line represents the fault during the inactive period, and the red dashed line represents the basement detachment. The red arrow indicates the direction of movement of the active faults, while the black arrow indicates the direction of movement of the inactive faults. The yellow pentagram represents the hypocenter of strong earthquake.

6. Conclusions

By interpreting high-resolution 2D seismic reflection profiles, a 3D geometric model of the pre-existing faults in the earthquake-affected area of the Pingyuan M_W 5.5 earthquake of August 6, 2023, was constructed. We analyzed the deep structural characteristics through velocity structure and provided a seismogenic model for the M_w 5.5 earthquake. The conclusion is as follows:

- (1) The 3D model of the Tuqiao Fault shows that the fault strikes NE and dips to the SE and that its depth ranges from 2.5 to 11 km. However, this fault occurrence does not match the focal mechanism solution. The depth of aftershocks is concentrated within 10–30 km, exceeding the development depth of the Tuqiao Fault. Moreover, the aftershock clusters trend to the NW, perpendicular to the Tuqiao Fault. Therefore, the Tuqiao Fault is not the seismogenic fault of the Pingyuan M_W 5.5 earthquake, and this study supports the previous results suggesting a deeper hypocenter location.

- (2) Based on the research results of other strong earthquakes in the eastern NCC, it is speculated that the seismogenic fault of the Pingyuan M_w 5.5 earthquake may be a high-angle strike-slip fault developed in the basement, which slid and ruptured under the current NEE compressive stress to produce this earthquake.
- (3) The velocity structure profile indicates the presence of a low-velocity layer at the bottom of the depression, potentially indicating the location of the detachment. The presence of the detachment separates two sets of structural systems: shallow extension faults and basement strike-slip faults. The seismogenic structure is unrelated to shallow structures but rather controlled by basement strike-slip faults. This seismogenic mode matches the structural model of the Xingtai earthquake, with decoupling of the upper and lower crust.
- (4) Because the depth of the hypocenter constrained from seismic data exceeds 10 km and the moment magnitude is less than 5.6, InSAR observations are likely unable to detect accurate coseismic deformation signals. Therefore, the coseismic deformation pattern remains unidentified, thus failing to provide helpful information about the fault kinematics of the earthquake.

Author Contributions: Conceptualization, R.L. and W.T.; formal analysis, G.L. and Y.Z.; investigation, D.H. and L.F.; data curation, G.L., writing—original draft preparation, P.S., R.L. and W.T.; writing—review and editing, R.L. and D.H.; supervision, R.L.; funding acquisition, R.L. All authors have read and agreed to the published version of the manuscript.

Funding: This study received financial support from the cooperation project of Institute of Geology, China Earthquake Administration (IGCEA1902), the National Key R&D Program of China (2021YFC3000600), and the National Natural Science Foundation of China (41872206).

Data Availability Statement: The raw data supporting the conclusions of this article will be made available by the authors on request. The seismic intensity map of the 2023 M_w 5.5 Pingyuan earthquake was accessed from <https://www.cea.gov.cn/> (accessed on 8 August 2023). The focal mechanism of the 2023 M_w 5.5 Pingyuan earthquake was obtained from the GCMT (<https://www.globalcmt.org/>; accessed on 5 August 2023), USGS (<https://www.usgs.gov/>; accessed on 5 August 2023), CENC (<https://news.ceic.ac.cn/>; accessed on 7 August 2023) and [Zhang et al., 2024] at [doi: 10.1016/j.eqs.2023.10.001], reference number [1], respectively. The relocated aftershocks of the 2023 M_w 5.5 Pingyuan earthquake were provided by [Zhang et al., 2024] at [doi: 10.1016/j.eqs.2023.10.001], reference number [1]. The seismic reflection profiles presented in this article are not readily available because Sinopec has not made it public. The velocity structure model can be accessed by contacting the corresponding author. The Sentinel-1 images were freely available through the Alaska Satellite Facility (<https://www.asf.alaska.edu/#/>; accessed on 1 February 2024).

Acknowledgments: Thanks to Zhe Zhang, Lisheng Xu, and Lihua Fang for providing the aftershock relocation data and focal mechanism solution. Thanks to Chenglong Li for providing the surface deformation from InSAR observation. The authors appreciate PetroChina for providing the seismic reflection profiles, drilling wells, and structural reflection maps.

Conflicts of Interest: The authors declare no conflicts of interest.

References

1. Zhang, Z.; Xu, L.S.; Fang, L.H. The M_w 5.5 Earthquake on August 6, 2023, in Pingyuan, Shandong: A Rupture on a Buried Fault. *Earthq. Sci.* **2024**, *1*, 1–12. [[CrossRef](#)]
2. Zhang, S.C. The feature of earthquake tectonics display by the seismicity pattern in north China. *Earthq. Res. Chin.* **1993**, *9*, 223–228.
3. Xu, J.; Wang, R.B.; Wang, C.H.; Song, C.Q. Preliminary study on two newly-generated seismotectonic zones in north and southwest China. *Northwest Seismol. J.* **1998**, *20*, 2–8.
4. Wang, C.Y.; Duan, Y.H.; Wu, Q.J.; Wang, Z.L. Exploration on the deep tectonic environment of strong earthquakes in north China and relevant research findings. *Acta Seismol. Sin.* **2016**, *38*, 511–549.
5. Gu, G.X. *Catalogue of Chinese Earthquakes 1831 B.C.–1969 A.D.* Scientific Publishing House: Singapore, 1983.
6. Wang, C.Y.; Zhang, X.K.; Lin, Z.Y.; Wu, Q.J.; Zhang, Y.S. Crustal structure beneath the Xingtai earthquake area in North China and its tectonic implications. *Tectonophysics* **1997**, *274*, 307–319. [[CrossRef](#)]

7. Xu, X.W.; Yu, G.H.; Wang, F.; Gu, M.L.; Sun, Z.G.; Liu, B.J.; You, H.C. Seismogenic model for the 1966 Xingtai earthquakes—Nucleation of new-born fault or strike-slip of pre-existing fault? *Earthq. Res. Chin.* **2000**, *16*, 364–378.
8. Huang, J.L.; Zhao, D.P. Seismic imaging of the crust and upper mantle under Beijing and surrounding regions. *Phys. Earth Planet. Inter.* **2009**, *173*, 330–348. [[CrossRef](#)]
9. Liu, G.D.; Shi, S.L.; Wang, B.J. The high-conductivity layer in the crust and its relationship with tectonic activity in north China. *Sci. Chin.* **1984**, *09*, 839–848.
10. Zeng, R.S.; Zhu, L.P.; He, Z.Q.; Ding, Z.F.; Sun, W.G. A seismic source model of the large earthquakes in north China extensional basin and discussion on the genetic processes of the extensional basin and earthquakes. *Acta Geophys. Sin.* **1991**, *34*, 288–301.
11. Liu, B.J.; Qu, G.S.; Sun, M.X.; Liu, K.; Zhao, C.B.; Xu, X.W.; Feng, S.Y.; Kou, K.M. Crustal structures and tectonics of Tangshan earthquake area: Results from deep seismic reflection profiling. *Seismol. Geol.* **2011**, *33*, 901–912.
12. Pavlis, N.K.; Holmes, S.A.; Kenyon, S.C.; Factor, J.K. The development and evaluation of the Earth Gravitational Model 2008 (EGM2008). *J. Geophys. Res. Solid Earth* **2012**, *117*, B04406. [[CrossRef](#)]
13. Zhang, S.C.; Zhao, J.; Diao, G.L. A preliminary study of the relation between focal faults and deep and shallow structures in north China area. *N. Chin. Earthq. Sci.* **1995**, *13*, 1–10.
14. Wei, W.B.; Tan, H.D.; Jin, S.; Deng, M.; Ye, G.F.; Deng, J.W.; Wan, Z.S. Conductivity structure of lithosphere in central north China: Magnetotelluric study of Yingxian-Shanghe profile. *Earth Sci.* **2002**, *27*, 645–650.
15. Zhang, Y.G.; Zheng, W.J.; Wang, Y.J.; Zhang, D.L.; Tian, Y.T.; Wang, M.; Zhang, Z.Q.; Zhang, P.Z. Contemporary deformation of the North China plain from global positioning system data. *Geophys. Res. Lett.* **2018**, *45*, 1851–1859. [[CrossRef](#)]
16. Li, X.N.; Hammond, W.C.; Pierce, K.D.; Bormann, J.M.; Zhang, Z.Q.; Li, C.Y.; Zheng, W.J.; Zhang, P.Z. Present-day strike-slip faulting and intracontinental deformation of North China: Constraints from improved GPS observations. *Geochem. Geophys. Geosyst.* **2023**, *24*, e2022GC010781. [[CrossRef](#)]
17. Zhu, W.L.; Mi, L.J.; Gong, Z.S. *Oil and Gas Accumulation and Exploration in the Bohai Sea Area*; Science and Technology Publishing Co., Ltd.: Beijing, China, 2009.
18. Li, D.S. Geology and structural characteristics of Bohai Bay, China. *Acta Pet. Sin.* **1980**, *1*, 6–20.
19. Liu, C.Y.; Huang, L.; Zhang, D.D.; Zhao, J.F.; Deng, Y.; Guo, P.; Huang, Y.J.; Wang, J.Q. Genetic causes of oil-rich and-poor reservoirs: Implications from two Cenozoic basins in the eastern North China Craton. *Sci. Chin. Earth Sci.* **2018**, *48*, 1506–1526. [[CrossRef](#)]
20. Qi, J.F.; Zhang, Y.W.; Lu, K.Z.; Yang, Q. Cenozoic tectonic evolution in Bohai Bay Basin province. *J. China Univ. Pet. Ed. Nat. Sci.* **1995**, *19*, 1–6.
21. Ren, J.; Tamaki, K.; Li, S.; Zhang, J. Late Mesozoic and Cenozoic rifting and its dynamic setting in Eastern China and adjacent area. *Tectonophysics* **2002**, *344*, 175–205. [[CrossRef](#)]
22. Hsiao, L.Y.; Graham, S.A.; Tilander, N. Seismic reflection imaging of a major strike-slip fault zone in a rift system: Paleogene structure and evolution of the Tan-Lu fault system, Liaodong Bay, Bohai, offshore China. *AAPG Bull.* **2004**, *88*, 71–97. [[CrossRef](#)]
23. Wang, M.J.; He, D.F.; Li, W.T.; Lu, R.Q.; Gui, B.L. Geometry, formation evolution and mechanism of Lanliao fault: The boundary of eastern Linqing depression, Bohaiwan Gulf. *Geol. Sci.* **2011**, *46*, 775–786.
24. Qi, J.F.; Yang, Q. Cenozoic structural deformation and dynamic processes of the Bohai Bay basin province, China. *Mar. Pet. Geol.* **2010**, *27*, 757–771. [[CrossRef](#)]
25. Li, S.Z.; Suo, Y.H.; Santosh, M.; Dai, L.M.; Liu, X.; Yu, S.; Zhao, S.J.; Jin, C. Mesozoic to Cenozoic intracontinental deformation and dynamics of the North China Block. *Geol. J.* **2013**, *48*, 543–560. [[CrossRef](#)]
26. Li, Z.H.; Qu, H.J.; Gong, W.B. Late Mesozoic basin development and tectonic setting of the northern North China Craton. *J. Asian Earth Sci.* **2015**, *114*, 115–139. [[CrossRef](#)]
27. Zhao, S.J.; Li, S.Z.; Niu, C.M.; Zhang, J.T.; Zhang, Z.; Dai, L.M.; Yang, Y.; Li, J.Y. Multistage structural superimposition and its control on buried hills in the Lyuda uplift zone, Bohai Bay Basin. *Oil Gas Geol.* **2023**, *44*, 1188–1202.
28. Qi, J.F.; Wang, D.R.; Chen, S.P.; Zhao, Y.B.; Cheng, X.S.; Xie, C.; Xu, Z.Q. Impact of geometry and kinematics of Lanliao fault on structural styles in Dongpu sag. *Oil Gas Geol.* **2006**, *27*, 451–459.
29. Zhu, R.X.; Chen, L.; Wu, F.Y.; Liu, J.L. Timing, scale and mechanism of the destruction of the North China Craton. *Sci. Chin. Earth Sci.* **2011**, *41*, 583–592. [[CrossRef](#)]
30. Su, P.; He, H.L.; Tan, X.B.; Liu, Y.D.; Shi, F.; Kirby, E. Initiation and Evolution of the Shanxi Rift System in North China: Evidence From Low-Temperature Thermochronology in a Plate Reconstruction Framework. *Tectonics* **2021**, *40*, e2020TC006298. [[CrossRef](#)]
31. Shen, F.M.; Wang, L.F.; Barbot, S.; Xu, J.H. North China as a mechanical bridge linking Pacific subduction and extrusion of the Tibetan Plateau. *Earth Planet. Sci. Lett.* **2023**, *622*, 118407. [[CrossRef](#)]
32. Sun, H.F. Application of velocity field construction method in a certain work area of Bohai Bay. *J. Yangtze Univ. Nat. Sci.* **2011**, *8*, 45–48.
33. Widess, M.B. How thin is a thin bed? *Geophysics* **1973**, *38*, 1021–1240. [[CrossRef](#)]
34. Zhang, H.J.; Thurber, C.H. Double-difference tomography: The method and its application to the Hayward fault, California. *Bull. Seismol. Soc. Am.* **2003**, *93*, 1875–1889. [[CrossRef](#)]
35. Yan, C.; Xu, L.S.; Zhang, X.; Li, C.L.; Xu, K.S. An inversion technique for mechanisms of local and regional earthquakes: Generalized polarity and amplitude technique (II): An application to real seismic events. *Chin. J. Geophys.* **2015**, *58*, 3601–3614.

36. Carena, S.; Suppe, J. Lack of continuity of the San Andreas Fault in southern California: Three-dimensional fault models and earthquake scenarios. *J. Geophys. Res.* **2004**, *109*, B04313. [[CrossRef](#)]
37. Lu, R.Q.; Xu, X.W.; He, D.F.; John, S.; Liu, B.; Wang, F.Y.; Tan, X.B.; Li, Y.Q. Seismotectonics of the 2013 Lushan Mw 6.7 earthquake: Inversion tectonics in the eastern margin of the Tibetan Plateau. *Geophys. Res. Lett.* **2017**, *16*, 8236–8243. [[CrossRef](#)]
38. Plesch, A.; Shaw, J.H.; Ross, Z.E.; Hauksson, E. Detailed 3D Fault Representations for the 2019 Ridgecrest, California, Earthquake Sequence. *Bull. Seismol. Soc. Am.* **2020**, *110*, 1818–1831. [[CrossRef](#)]
39. Wang, M.J.; Zhang, X.H.; Zhang, Y.B.; He, D.F.; Li, W.T. Restoration of denuded formation thickness and prototype basin of early to middle jurassic in eastern Linqing depression. *Spec. Oil Gas Reserv.* **2012**, *19*, 17–21.
40. Werner, C.; Wegmüller, U.; Strozzi, T.; Wiesmann, A. Gamma SAR and interferometric processing software. In Proceedings of the ERS-ENVISAT Symposium, Gothenburg, Sweden, 16–20 October 2000; Volume 1620, p. 1620.
41. Yagüe-Martínez, N.; Prats-Iraola, P.; Rodriguez Gonzalez, F.; Brcic, R.; Shau, R.; Geudtner, D.; Eineder, M.; Bamler, R. Interferometric Processing of Sentinel-1 TOPS Data. *IEEE Trans. Geosci. Electron.* **2016**, *54*, 2220–2234. [[CrossRef](#)]
42. Daout, S.; Sudhaus, H.; Kausch, T.; Steinberg, A.; Dini, B. Interseismic and Postseismic Shallow Creep of the North Qaidam Thrust Faults Detected with a Multitemporal InSAR Analysis. *J. Geophys. Res. Solid Earth* **2019**, *124*, 7259–7279. [[CrossRef](#)]
43. Tadono, T.; Ishida, H.; Oda, F.; Naito, S.; Minakawa, K.; Iwamoto, H. Precise Global DEM Generation by ALOS PRISM. *ISPRS Ann. Photogramm. Remote Sens. Spat. Inf. Sci. II* **2014**, *2*, 71–76. [[CrossRef](#)]
44. Goldstein, R.M.; Werner, C.L. Radar interferogram filtering for geophysical applications. *Geophys. Res. Lett.* **1998**, *25*, 4035–4038. [[CrossRef](#)]
45. Werner, C.; Wegmüller, U.; Strozzi, T.; Wiesmann, A. Processing strategies for phase unwrapping for InSAR applications. In Proceedings of the EUSAR 2002, Cologne, Germany, 4–6 June 2002; pp. 4–6.
46. Zhu, Z.P.; Zhang, X.K.; Gai, Y.J.; Zhang, J.S.; Nie, W.Y.; Shi, J.H.; Zhang, C.K.; Ruan, H. Study on the slow velocity structure of the crust in the Xingtai earthquake source area and adjacent areas. *Acta Seismol. Sin.* **1995**, *17*, 328–334.
47. Deng, Q.H.; Zhang, M.S.; Zhan, Y.Y.; Liu, G.D.; Zhao, G.Z.; Tang, J. The observation of electromagnetic array profiling and electrical characteristics of the crust in Xingtai M_S 7.2 earthquake area. *Acta Geophys. Sin.* **1998**, *41*, 218–225.
48. Ding, G.Y.; Lu, Y.C. Discussion on the basic characteristics of new construction and deformation in the north China block. *N. Chin. Earthq. Sci.* **1983**, *1*, 1–9.
49. Zheng, B.H.; Ma, Z.J. The faulting-block tectonics and structural detachment between middle and lower crust in the north part of north China. *Earthq. Res. Chin.* **1991**, *7*, 3–12.
50. Wang, C.Y.; Zhang, X.K.; Wu, Q.J.; Zhu, Z.P. Seismic evidence of detachment in north China basin. *Acta Geophys. Sin.* **1994**, *37*, 613–620.
51. Liu, G.D.; Gu, Q.; Shi, S.L.; Sun, J.; Shi, Z.S.; Liu, J.H. The electrical structure of the crust and upper mantle and its relationship with seismicity in the Beijing-Tianjin-Tangshan region and adjacent area. *Acta Geophys. Sin.* **1983**, *26*, 149–157.
52. Duan, Y.H.; Wang, F.Y.; Zhang, X.K.; Lin, J.Y.; Liu, Z.; Liu, B.F.; Yang, Z.X.; Guo, W.B.; Wei, Y.H. Three dimensional crustal velocity structure model of the middle-eastern North China Craton (HBCrust1.0). *Sci. Chin. Earth Sci.* **2016**, *46*, 845–856. [[CrossRef](#)]
53. Qu, G.S.; Zhang, H.; Ye, H. The principle stress orientations by the borehole breakouts in Huanghua depression. *N. Chin. Earthq. Sci.* **1993**, *11*, 9–18.
54. Wang, M.; Shen, Z.K. Present-Day Crustal Deformation of Continental China Derived from GPS and Its Tectonic Implications. *J. Geophys. Res. Solid Earth* **2020**, *125*, e2019JB018774. [[CrossRef](#)]
55. Yang, S.H.; Pan, J.W.; Li, H.B.; Shi, Y.L. Present-day Upper-crustal Strain Rate Field in Southeastern Tibet and its Geodynamic Implications: Constraints from GPS Measurements with ABIC Method. *Acta Geol. Sin.* **2024**, *1*, 265–275. [[CrossRef](#)]
56. Yin, A. Cenozoic tectonic evolution of Asia: A preliminary synthesis. *Tectonophysics* **2010**, *488*, 293–325. [[CrossRef](#)]
57. Qi, J.F. Two tectonic systems in the Cenozoic Bohai Bay basin and their genetic interpretation. *Geol. Chin.* **2004**, *31*, 15–22.
58. Xu, J.; Zhou, B.G.; Ji, F.J.; Gao, Z.W.; Chen, G.G.; Sun, J.B. Features of seismogenic structures of great earthquakes in the Bohai Bay basin area, north China. *Seismol. Geol.* **2012**, *34*, 618–636.
59. Wang, C.Y.; Wu, Q.J.; Duan, Y.H.; Wang, Z.L.; Lou, H. Crustal and upper mantle structure and deep tectonic genesis of large earthquakes in north China. *Sci. Chin. Earth Sci.* **2017**, *47*, 684–719. [[CrossRef](#)]
60. Xu, H.G.; Fan, X.P.; Ran, Y.K.; Gu, Q.P.; Zhang, P.; Li, L.M.; Zhao, Q.G.; Wang, J.Y. New evidences of the Holocene fault in Suqian segment of the Tanlu fault zone discovered by shallow seismic exploration method. *Seismol. Geol.* **2016**, *38*, 111–129.
61. Tan, X.; Liang, K.; Ma, B.Q.; He, Z.T.; Liu, G.Y.; Li, Z.P.; Li, L.; Zhao, J.X. A catastrophic, buried fault-generating earthquake: The 1937 M 7.0 Heze earthquake in the south-central North China Plain. *J. Struct. Geol.* **2023**, *177*, 104988. [[CrossRef](#)]
62. Zhang, Z.L.; Li, Q.Z.; Gu, J.C.; Jin, Y.M.; Yang, M.Y.; Liu, W.Q. The fracture processes of the Tangshan earthquake and its mechanical analysis. *Acta Seismol. Sin.* **1980**, *2*, 3–21.

Disclaimer/Publisher’s Note: The statements, opinions and data contained in all publications are solely those of the individual author(s) and contributor(s) and not of MDPI and/or the editor(s). MDPI and/or the editor(s) disclaim responsibility for any injury to people or property resulting from any ideas, methods, instructions or products referred to in the content.